

Rheology of dense fiber suspensions: Origin of yield stress, shear thinning, and normal stress differences

Monsurul Khan,¹ Rishabh V. More ,¹ Luca Brandt,² and Arezoo M. Ardekani ¹

¹*Department of Mechanical Engineering, Purdue University, Indiana 47905, USA*

²*FLOW, Department of Engineering Mechanics, KTH, Royal Institute of Technology, Stockholm, Sweden*



(Received 12 September 2022; accepted 31 May 2023; published 27 June 2023)

We explain the origins of yield stress, shear thinning, and normal stress differences in rigid fiber suspensions. We investigate the interplay between the hydrodynamic, noncontact attractive and repulsive, and interfiber contact interactions. The shear-thinning viscosity and finite yield stress obtained from the Immerse Boundary Method simulations are in quantitative agreement with experimental results from the literature. In this study, we show that attractive interactions result in yield stress and shear thinning rheology in the suspensions of rigid fibers. This is an important finding, given the ongoing discussion regarding the origin of the yield stress for suspensions of fibers. The ability of the proposed model to quantitatively predict the rheology is not limited to only shear thinning and yield stress but also extends to normal stresses.

DOI: [10.1103/PhysRevFluids.8.064306](https://doi.org/10.1103/PhysRevFluids.8.064306)

I. INTRODUCTION

Fiber suspensions are widely encountered in natural and industrial applications, with examples in paper and pulp production, biomass solutions, and chemical processing [1–5]. Under shear, these suspensions display several non-Newtonian properties such as the Weissenberg effect [6,7], shear thinning [8–10], nonzero normal stresses [11,12], and yield stress [10]. Specifically, shear thinning in fiber suspensions has been an active area of research, and consequently, the literature provides many phenomenological explanations, such as the increase in the effective particle size due to the presence of electric double layer [13], excluded volume interactions between rigid fibers [14], elastic bending of flexible micro-sized or nano-sized fibers [15,16], fiber aggregation [17], and nonlinear lubrication force [18]. However, not much attention has been paid in utilizing these phenomenological explanations to develop robust numerical models that can capture the underlying physics and consequently, predict suspension rheological properties.

Non-Newtonian rheology arises from a variety of interactions such as hydrodynamics, cohesive [19,20], contact [21,22], and is influenced by the physical properties of fibers, e.g., roughness, shape, size distribution, etc. [23,24]. Each of these interactions leads to a corresponding stress scale that is competing with hydrodynamic stress. The competition between these stress scales could lead to a rate-dependent rheological behavior [25,26]. Among these different interactions between fibers, the influence of short-range hydrodynamic forces and direct mechanical contact has been understood through theoretical modeling [27,28] and numerical simulations [21,29]. However, there is little documentation on the study of fiber suspensions with noncontact interactions, even though van der Waals forces [30], depletion forces due to dissolved noninteracting polymers [31], presence of external fields [32] can lead to attractive forces between fibers. Therefore, it is crucial to understand the effect of attractive and repulsive forces in fiber suspensions as they produce nonlinear scaling of the shear stress with shear rate. Earlier efforts, including experiments on an attractive system with nanofibers, show that the interplay between electrostatic repulsion and the van der Waals attraction governs the degree of fiber flocculation and yielding behavior [33,34]. Moreover, shear thinning was

observed due to adhesive interactions in the suspension of rigid microsized rodlike particles such as polyamide (PA) [35] and ceramic fibers [36]. However, the role of noncontact interactions remained unclear. Lately, a theoretical model of aggregated fiber suspensions, considering the adhesive force between fibers, shows a good match with experiments on the rigid fiber suspensions [10,37]. This model included fitting parameters, which were obtained from experimental data. None of these explanations describe the behavior of normal stresses, and so their applicability is limited.

The apparent yield stress, i.e., the minimum stress required to begin the flow, is considered one of the most important rheological properties of fiber suspensions. The yield stresses in the suspensions rise as the volume fraction increases, and they are more noticeable for greater aspect ratios [12,38]. A recent theoretical model that considered attractive interactions between fibers in the dilute regime predicted the Bingham law for the shear stress, with apparent yield stress proportional to the square of volume fraction (ϕ^2) [37]. The shear stress for suspensions of larger-sized rigid fibers also follows the Bingham law, but the yield stress rises with higher power laws in ϕ than predicted in previous studies [38]. The origin of yield stress has been attributed to adhesive contacts even though the fiber size was large [35]. As pointed out in Tapia *et al.* [38], recent experimental studies failed to come to a conclusion on whether the fiber size or the attractive forces are responsible for the yield stress and mentioned the necessity of further investigation to pinpoint the origin of the yield stress.

As there is no clear explanation of the shear thinning and yield stress in fiber suspensions, we provide a predictive model in this paper. Our proposed model incorporates short-range interactions via attractive and repulsive interactions along with contact interactions that quantitatively capture shear thinning rheology and yield stress in the fiber suspensions, and elucidate the effect of noncontact interactions. Moreover, our model not only explains the yield stress and shear thinning behavior but also accurately predicts the normal stresses, which further strengthens the validity of our model. Lastly, we demonstrate the versatility of the proposed model by capturing the effect of changing surface properties by accurately modeling the contact dynamics. To the best of the authors' knowledge, this is the first computational study to quantitatively capture the experimentally observable rheological behavior (relative viscosity η_r , first normal stress coefficient α_1 , second normal stress coefficient α_2 , and yield stress σ_y) of fiber suspensions and demonstrate the underlying physical mechanism.

II. SIMULATION METHODOLOGY

We perform direct numerical simulations of neutrally buoyant fibers with aspect ratio $A = l/d$, where l is the length and d is the diameter of the fiber, in a shear flow generated by the top and bottom parallel walls moving in opposite directions with a velocity $U_\infty = \dot{\gamma}l$ generating an imposed shear rate $\dot{\gamma}$, as shown in Fig. 1. Here, l is the length of the fiber.

The suspending fluid is incompressible Newtonian with a viscosity η , and its flow is governed by the Navier-Stokes equations written in a dimensionless form:

$$\frac{\partial \mathbf{u}}{\partial t} + \nabla \cdot (\mathbf{u} \otimes \mathbf{u}) = -\nabla p + \frac{1}{Re} \nabla^2 \mathbf{u} + \mathbf{f}, \quad (1)$$

$$\nabla \cdot \mathbf{u} = 0, \quad (2)$$

where \mathbf{u} is the dimensionless velocity field, p is the dimensionless pressure, \mathbf{f} is the dimensionless volume force to account for the suspending fibers, and $Re = \rho \dot{\gamma} l^2 / \eta$ is the Reynolds number, where ρ is the fluid density, l is the characteristic length scale which is also the fiber length. We model the fibers as in-extensible slender bodies. So, their motion for the neutrally buoyant case is described by the Euler-Bernoulli beam equation as [24]

$$\frac{\partial^2 \mathbf{X}}{\partial t^2} = \frac{\partial^2 \mathbf{X}_{\text{fluid}}}{\partial t^2} + \frac{\partial}{\partial s} \left(T \frac{\partial \mathbf{X}}{\partial s} \right) - B \frac{\partial^4 \mathbf{X}}{\partial s^4} - \mathbf{F} + \mathbf{F}^f, \quad (3)$$

where s is the curvilinear coordinate along the fiber, $\mathbf{X} = (x(s, t), y(s, t), z(s, t))$ is the position of the Lagrangian points on the fiber axis, T is the tension, B is the bending rigidity, \mathbf{F} is the fluid-solid

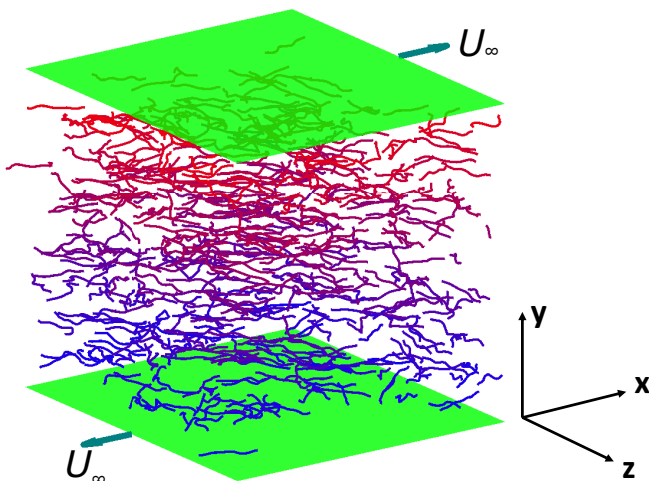


FIG. 1. Simulation setup of the shear flow of a fiber suspension. The top and bottom walls move with velocities $U_\infty = \dot{\gamma}l$ in the directions shown by the arrows. $\dot{\gamma}$ is the imposed shear rate, and l is the length of the fibers. Here, x is the flow direction, y is the gradient direction, and z is the vorticity direction.

interaction force, and \mathbf{F}^f is the net interfiber interaction. The fibers are considered inextensible, expressed as [39,40]

$$\frac{\partial \mathbf{X}}{\partial s} \cdot \frac{\partial \mathbf{X}}{\partial s} = 1. \quad (4)$$

We use the immersed boundary method (IBM) [41] to couple the motion of fluid and solid fibers. For the details of the numerical method, readers are referred to the Supplemental Material [42].

In the numerical simulation, the hydrodynamic interactions are well resolved with IBM. However, a fine Eulerian mesh is required to capture the short-range lubrication interactions that increase the computational cost. So, we use lubrication correction to calculate the short-range lubrication interactions when the inter-fiber gap is below a certain threshold. In addition, various noncontact and contact interactions can be readily incorporated in the net interfiber interaction, $\mathbf{F}^f = \mathbf{F}^{\text{lc}} + \mathbf{F}^c + \mathbf{F}^{\text{cons}}$, where \mathbf{F}^f is split into the lubrication correction \mathbf{F}^{lc} [43], contact force \mathbf{F}^c , noncontact conservative force $\mathbf{F}^{\text{cons}} = \mathbf{F}^A + \mathbf{F}^R$, where \mathbf{F}^A is the van der Waals attractive force, and \mathbf{F}^R is the repulsive force of electrostatic origin. The implementation details of the lubrication correction \mathbf{F}^{lc} can be found in the Supplemental Material [42]. The expressions for attractive and repulsive interactions are readily available from theoretical analyses and previous experimental measurements [36,44]. The attractive force of van der Waals origin acts normally to the fiber surfaces and is modeled as $|\mathbf{F}^A| = F_A/(h^2 + H^2)$, where h is the interfiber surface separation and H is a small number, which is fixed to 0.01 to prevent the divergence in $|\mathbf{F}^A|$ when $h \rightarrow 0$ (during contact). The strength of the attraction is controlled by F_A , which determines the magnitudes of the attractive force in contact. The repulsive force \mathbf{F}^R also acts in the normal direction to the fiber surfaces but is opposite to the attractive force. \mathbf{F}^R decays with the interfiber separation h over the Debye length κ as $|\mathbf{F}^R| = F_R \exp(-h/\kappa)$ [20,25]. The contact between the fibers occurs when the interfiber separation distance h becomes smaller than the height of surface asperity h_r , as shown in Fig. 2. Specifically, the single-asperity model of surface roughness has been widely used owing to its simplicity and effectiveness [22,45–48]. Hence, we take the same approach and model the asperity as a hemispherical bump on the fiber surface. Actual asperities might not be just hemispherical and can come in various geometries [49]. However, on average, we can model their behavior by approximately assuming them hemispherical as routinely done in the tribology literature [50].

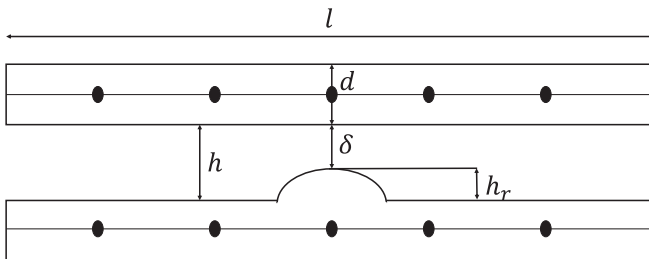


FIG. 2. A sketch of the roughness model, l and d are the length and diameter of the fiber, respectively, h_r is the asperity height, and $\delta = h - h_r$ is the surface overlap. Contact occurs when $\delta \leq 0$. Dots along the axes of the fibers indicate Lagrangian points.

Finally, we split the contact force \mathbf{F}^c into the tangential (\mathbf{F}_t^c) and normal (\mathbf{F}_n^c) components. The normal contact force is modeled using a Hertz law, $|\mathbf{F}_n^c| = -k_n|\delta|^{3/2}$, where $\delta = h_r - h$ is the asperity deformation, and k_n is the normal stiffness, which is a function of the fiber material properties [22,48]. The Coulomb's friction law gives the tangential force, $|\mathbf{F}_t| = \mu|\mathbf{F}_n|$, where the coefficient of friction $\mu = 0.4$ in the current work unless mentioned otherwise. The typical value of μ is 0.3–0.5 as measured experimentally for the polymer fibers [51,52]. Even though little is known about the friction mechanics at the nanoscale, the Coulomb friction allows a correct prediction for flows of colloidal nanoparticles [53] or hard-sphere suspensions [45]. We use a repulsive force magnitude as the characteristic force to scale the various forces. Consequently, the characteristics shear rate scale is $\dot{\gamma}_0 = F_R/\pi\eta d^2$ and the corresponding shear stress scale is $\sigma_0 = F_R/\pi d^2$.

We calculate the bulk stress (Σ_{ij}) by volume averaging the viscous fluid stress and stress generated by the presence of fibers [54] and interfiber interactions. There are three main contributions to the bulk stress: (1) the hydrodynamic contribution, Σ_{ij}^h , (2) the contact contribution, Σ_{ij}^c , and (3) the noncontact contribution, Σ_{ij}^{nc} . The calculation of bulk stress, including different contributions, is described in the Supplemental Material [42]. Rheological properties can be quantified from the bulk stress, e.g., the relative viscosity, $\eta_r = \sigma_{xy}/\eta\dot{\gamma}$, where σ_{xy} is the total shear stress in the suspension. As shown in Fig. 1, x is the flow direction, y is the gradient direction, and z is the vorticity direction. Hence, the first and second normal stress coefficients are defined as $\alpha_1(\phi) = (\sigma_{xx} - \sigma_{yy})/\sigma$ and $\alpha_2(\phi) = (\sigma_{yy} - \sigma_{zz})/\sigma$, where ϕ is the volume fraction of fibers defined as $\phi = \frac{N\pi}{4\nu(A)^2}$, where $\nu = V/l^3$. Here V is the total volume ($5l \times 8l \times 5l$) of the simulation cell, and N is the total number of fibers in the simulation domain. Moreover, the dimensionless fiber bending rigidity \tilde{B} , is defined as $\tilde{B} = EI/\eta\dot{\gamma}l^4$, where E is the modulus of elasticity of the fiber and I the second moment of inertia around the fiber axis.

III. RESULTS AND DISCUSSION

A. Shear-rate-dependent rheology

We start our analysis by demonstrating the accuracy of the proposed model by directly comparing the calculated relative viscosity and shear stress with experimental measurements of neutrally

TABLE I. Characteristics of the fiber suspension used in the study of Bounoua *et al.* [37].

Material	Length l (μm)	Diameter d (μm)	Aspect ratio A	Density (g/cm^3)
	500	15.2 ± 0.5	33 ± 1.0	1.340 ± 0.001
	500	27.8 ± 0.5	18 ± 0.5	1.090 ± 0.001
PA	300	30.0 ± 1.0	10	1.090

TABLE II. Range of parameters explored in this study.

Re	A	\tilde{B}	$\frac{\dot{\gamma}}{\dot{\gamma}_0}$	ϕ
1	10,18,33	5.0	0.01–100	0.01–0.25

buoyant polyamide (PA) fiber suspensions, which exhibit a yield stress and shear thinning viscosity [10,37]. PA fibers were suspended in a Newtonian fluid (a mixture of UCON oil 75H90000 in distilled water) at different volume fractions ranging from 1% to 17%, depending on the fiber aspect ratio. Moreover from the experimental study, we find the Reynolds number $\text{Re} = 4 \times 10^{-3}$, aspect ratio $A = 10, 18, 33$, and dimensionless bending rigidity \tilde{B} in the range of $4 - 4 \times 10^4$ [19,37]. The roughness (h_r) of the fibers has been measured using atomic force microscopy, having values $h_r = 5 \pm 2$ nm and $h_r = 14 \pm 4$ nm for the aspect ratio $A = 18$ and $A = 33$, respectively [10]. The dimensionless roughness calculated as $\epsilon_r = h_r/d$ is 0.0003 and 0.001 for aspect ratios 18 and 33, respectively, corresponds to smooth fibers. The details of the fibers and suspending fluid used in the experiment is reported in Table I [10]. In our numerical simulations, due to time-step constraint at very low Reynolds number, we fix $\text{Re} = 1$. Moreover, we have chosen the value of the fiber bending rigidity $\tilde{B} = 5.0$, for which fiber remains rigid in the numerical simulations. Finally, the roughness of the fibers is fixed to $\epsilon_r = 0.003$ for aspect ratio 10 and 18, and $\epsilon_r = 0.001$ for aspect ratio 33 to mimic the experimental fibers. The parameters chosen in our simulations are reported in Table II.

The numerical and experimental comparison of the relative viscosity and flow curves in Figs. 3(a) and 3(b) for the aspect ratios $A = 18$ and $A = 33$ shows that the proposed computational model does an excellent job capturing the rate-dependent rheological behavior. We notice that the high shear plateaus of the relative viscosity shift to higher shear rate values as the volume fraction increases. We consider the bending rigidity, \tilde{B} of fiber to be 5.0, which ensures negligible bending of the fiber that mimic PA fibers used in the experiment. To illustrate that the fibers in the simulations remain rigid as in the experimental setting, we have calculated the mean distance between two ends of each fiber, where the average is performed over time and the number of fibers. Also, to visualize, we display the fibers collocated with their center positioned at the origin of the axis, i.e., we shift their centers to the origin and plot fibers in the same graph as shown in Fig. 4. Here, the solid red line

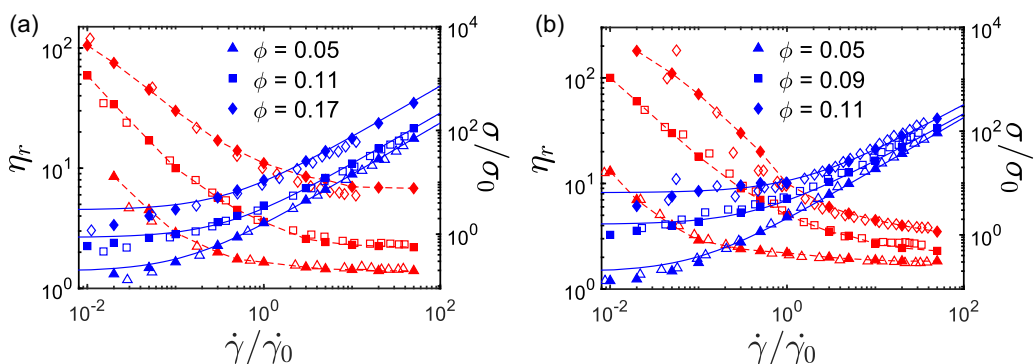


FIG. 3. Experimental and numerical comparison of relative viscosity η_r (red symbol) and shear stress (blue symbol) versus the nondimensional shear rate at different volume fractions: fibers with an aspect ratio (a) $A = 18$; (b) $A = 33$. Filled symbols with dashed lines show the numerical data. Hollow symbols correspond to experiments, and solid lines in the shear stress curve denote the best fit with the Herschel–Bulkley model equation (5) for numerical data. Experimental shear rate and shear stress have been scaled by $\dot{\gamma}_0 = 2.5$ and $\sigma_0 = 0.7$, respectively. Inclusion of attractive and repulsive interactions along with interfiber contact interactions quantitatively reproduce the experimentally observed shear-thinning viscosity and shear stress [10].

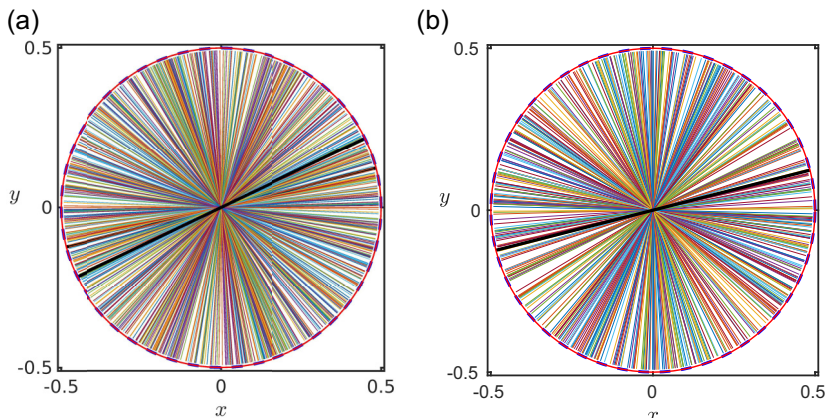


FIG. 4. Colocated filaments projected on the shear plane for dimensionless shear rate (a) $\dot{\gamma}/\dot{\gamma}_0 = 0.01$, (b) $\dot{\gamma}/\dot{\gamma}_0 = 5$. The solid black line shows the average orientation of the fibers with respect to the wall. As the shear rate increases, fibers align more with the flow direction. The solid red line represents the circles with a diameter equal to the fiber length; and the blue dashed line is the circle with a diameter equal to the mean end-to-end distance for each case. The solid red line coincides with the blue dashed line, confirming that the fibers are rigid. All simulations are performed with volume fraction $\phi = 0.17$, and aspect ratio $A = 18$.

represents the circles with a diameter equal to the fiber length, and the blue dashed line is the circle with a diameter equal to the mean end-to-end distance for each case. The solid red line coincides with the blue dashed line, confirming that the fibers remain rigid. Moreover, we calculate the average orientation of the fiber with the flow direction as shown by the solid black line. As the shear rate increases, they align more with the flow direction [Figs. 4(a) and 4(b)], eventually decreasing the hydrodynamic contributions. Moreover, the overall resistance of the suspension decreases as a result of the alignment of the fibers more with the flow direction, lowering the relative viscosity. The origin of the shear thinning rheology will be explained in detail in the next section. From the computational flow curve (blue symbols) in Fig. 3, we observe that our numerical model does reproduce the low shear plateau, ($\frac{\dot{\gamma}}{\dot{\gamma}_0} < 0.10$), reminiscent of the yield stress and the linear segments of the flow curve at high dimensionless shear rates, ($\frac{\dot{\gamma}}{\dot{\gamma}_0} > 0.10$), observed in experiments. Due to this trend in the flow curve, the shear stress of the fiber suspensions can be described by the Herschel–Bulkley model as

$$\frac{\sigma}{\sigma_0} = \sigma_y + k \left(\frac{\dot{\gamma}}{\dot{\gamma}_0} \right)^n, \quad (5)$$

where σ_y is the dimensionless yield stress, k is the consistency index, and $n < 1$ is the shear thinning index. The solid lines in the flow curve (Fig. 3) demonstrate the best fit to the Herschel–Bulkley model for the computational data. The yield stress σ_y and the fitting parameter are provided in Table III. The yield stress for a given volume fraction is higher for fibers with a higher aspect ratio. Furthermore, as the volume fraction rises, the yield stress increases for a fixed aspect ratio. To analyze the concentration dependence of the yield stress, we plot the yield stress for different volume fractions in Fig. 5(a). It is clear that σ_y has a weak dependence on ϕ in dilute and semidilute regimes ($\phi \leq 0.10$ for $A = 10$ and $\phi \leq 0.05$ for $A = 18$); the dependence is seen to increase more rapidly with ϕ for concentrated regimes.

Moreover, to measure the possibility of the nematic ordering in the suspension, we calculate Onsager’s dimensionless concentration, defined as $C = 0.25\pi L^2 DV$, which is numerically equivalent to solid volume fraction ϕ multiplied by the aspect ratio A ($C = A\phi$) [55–57]. The dimensionless concentrations for isotropic (C_I , above which the isotropic phase is not stable) and nematic phase

TABLE III. Herschel-Bulkley parameters [Eq. (5)] for different volume fractions for aspect ratios 18 and 33.

A	ϕ	σ_y	k	n
18	0.05	0.1898	1.409	0.9975
	0.11	0.8571	2.301	0.9865
	0.17	2.9280	7.608	0.9851
	0.05	0.1903	1.882	0.9935
	0.09	1.5870	3.028	0.9255
33	0.11	6.5000	4.580	0.9218

(C_N , above which the nematic phase is stable) are calculated to be 3.29 and 4.19, respectively. For concentration between $C_I < C < C_N$, isotropic and nematic phases coexist [58,59]. The maximum volume fraction we have simulated for our study is 0.25, 0.19, and 0.09 for aspect ratio $A = 10, 18$, and 33, respectively. The corresponding Onsager's dimensionless concentration can be calculated as 2.50, 3.42, and 2.97 for $A = 10, 18$, and 33, respectively. So, we can conclude that only for $A = 18$ we have performed a simulation in a state when the isotropic phase is unstable. Other cases we have simulated can be considered isotropically stable. More discussion on nematic order parameter [60] can be found in Supplemental Material Fig. S7 [42]. Since nematic phase stability is not the focus of the study, hence not pushed further. The dependence of yield stress σ_y on ϕ can be well described using the relation proposed by [61]

$$\sigma_y = \sigma_c \left[\frac{\frac{\phi}{\phi_y^0} - 1}{1 - \frac{\phi}{\phi_y^m}} \right]^{\frac{1}{\beta}}, \quad (6)$$

where ϕ_y^0 is a threshold volume fraction, from which the architecture of a concentrated suspension can sustain some external forces, and a certain stress has to be imposed on to initiate the flow [61]. In addition, ϕ_y^m denotes the maximum volume fraction at which the yield stress diverges and beyond which the suspension does not move at any applied stress. So, we need a model with two characteristic volume fractions to capture the variation of yield stress with volume fraction. The fitting parameters are provided in Table IV. The threshold volume fraction ϕ_y^0 and maximum volume

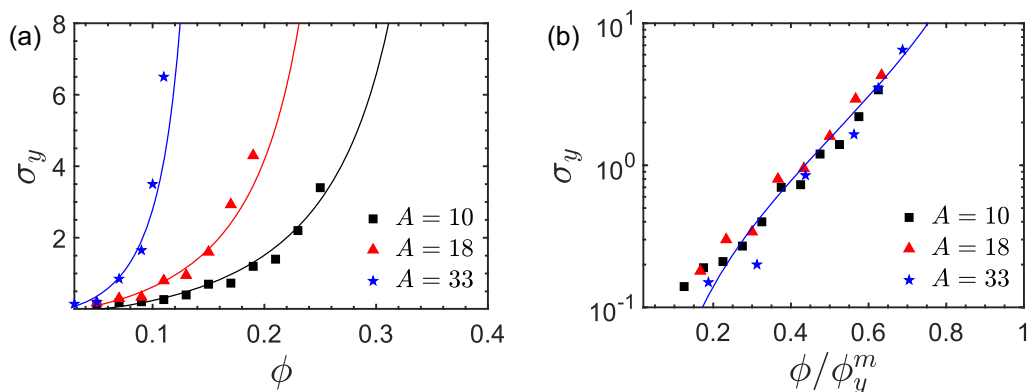


FIG. 5. (a) Yield stress σ_y as a function of volume fraction. The solid line shows the best fit of the data to Eq. (6). (b) Yield stress σ_y as a function of rescaled volume fraction. Rescaling the volume fraction ϕ by ϕ_y^m leads to the collapse of data (solid line in Fig. 5(b)) indicating that it is the ratio of ϕ to ϕ_y^m that determines the suspension rheology.

TABLE IV. Fitting parameters of Eq. (6) for aspect ratios, $A = 10, 18,$ and 33 .

A	ϕ_y^0	ϕ_y^m	σ_c	β
10	0.05	0.40	0.17	0.8200
18	0.03	0.30	0.14	0.8015
33	0.017	0.16	0.09	0.7473

fraction ϕ_y^m decreases with the aspect ratio. The percolation threshold volume fraction is considered to be $0.7/A$ [62,63]. For aspect ratio $A = 10, 18,$ and 33 , the percolation threshold is calculated as $0.070, 0.370,$ and 0.021 , respectively. For the aspect ratios studied in this study, ϕ_y^0 is in the dilute regime, and below the threshold of the percolation limit. However, as the volume fraction increases over $0.7/A$, we expect percolation in the suspension.

From the data presented in Table IV, we notice that for $A = 10, 18,$ and 33 , $A\phi_y^m = 4.0, 5.4,$ and 5.0 , respectively. The relatively constant $A\phi_y^m$ value for $A = 18$ and 33 matches with Philipse [58] prediction gathered from a large number of experimental systems that the packing volume ϕ_y^m obeys $A\phi_y^m = 5.4 \pm 0.2$ for $A \geq 20$ [58]. Moreover, for $A = 10$, $A\phi_y^m$ is found to be 4.0 , which also matches Philipse experimental data [58,64]. So, according to the Philipse [58] study, we can conclude that the jamming of the system studied here is a geometrical property and jams at the frictionless random close packing limit of fiber. Moreover, we have used a small value for coefficient of friction ($\mu = 0.4$), hence it can be considered almost frictionless. A higher coefficient of friction, which can arise due to higher roughness on the fiber surface, results in a lower jamming fraction than the frictionless one. We have investigated the effect of roughness on jamming volume fraction in our previous study [21].

Figure 5(b) shows the data after rescaling the volume fractions of Fig. 5(a) by ϕ_y^m , which leads to the collapse of the data. Hence, the ratio of ϕ to the maximum volume fraction ϕ_y^m at which the yield stress diverges determines the suspension rheology. Hence, ϕ/ϕ_y^m can be used as a design parameter for tuning the fiber suspension rheology, as it is easier to measure and control compared to other parameters, like size distribution, roughness, and friction in real-world suspensions. In the next section, we focus on the origin of shear thinning and yield stress to understand the underlying mechanism and control the rheological response.

B. Origin of shear thinning and yield stress

We focus on the origin of yield stress, especially with increasing the attractive force, in an attempt to acquire a more mechanistic understanding of the shear thinning behavior. Figure 6 depicts the effect of varying the attractive force magnitude on the rheology of a fiber suspension. The aspect ratio and volume fraction are fixed at 18% and 17% , respectively. We do not observe yield stress in the suspension for $F_A = 0$. With an increase in the magnitude of the attractive force, the slope of the shear thinning curve at low shear rate increases, which leads to a rise in the yield stress, as shown in Fig. 6(a). With the increase in F_A , the separation distance h below which the conservative force is repulsive decreases (shown in Supplemental Material Fig. S3 [42]). At a sufficiently high attractive force, the position of zero force and cutoff separation for lubrication ($d/4$) are the same, bringing fibers into direct frictional contact. These frictional contacts can withstand applied shear stress, increasing the yield stress and viscosity. The role of noncontact interactions can be better understood by separating the hydrodynamic, contact, and noncontact (attractive+repulsive) contributions to viscosity [Figs. 6(b) and 6(c)]. The hydrodynamic contribution to the overall viscosity is negligible for the conditions under consideration. The data plotted here shows an increase in the contact contribution to the relative viscosity as the attractive force increases. At low attractive force values, the noncontact forces contribute the most to the overall viscosity, while contact contributions take over at higher shear rates. Even though the attractive force is the cause of the yield stress and must

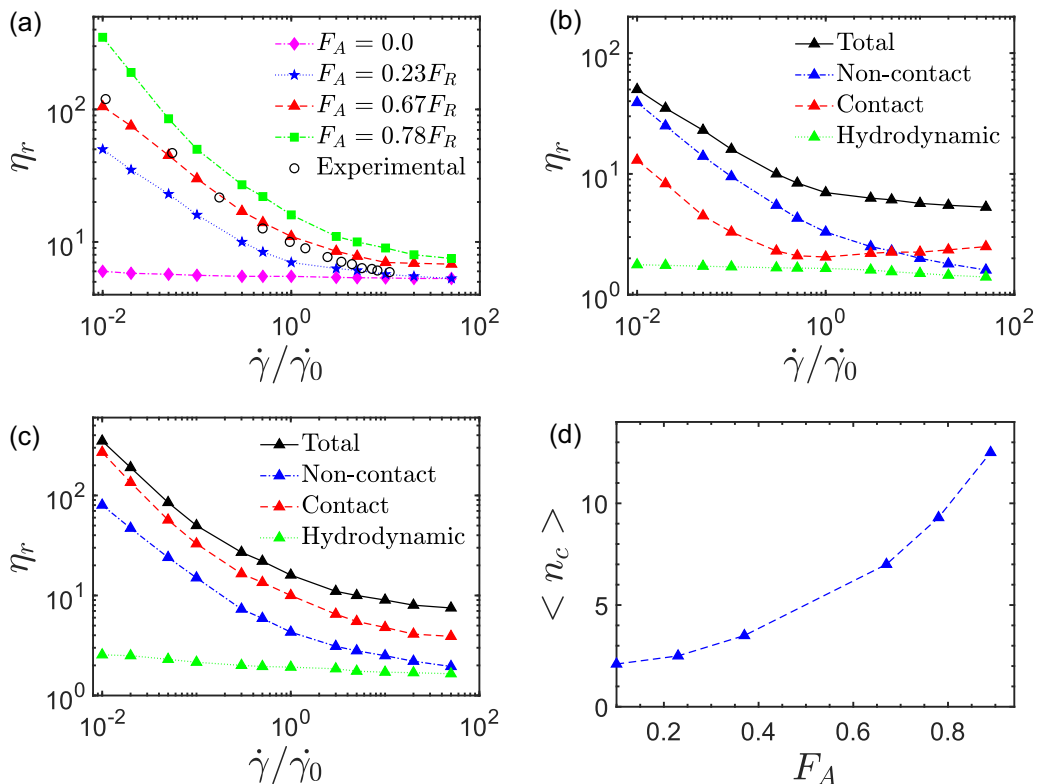


FIG. 6. (a) Relative viscosity plotted as a function of dimensionless shear rate for different values of attractive force F_A . Total relative viscosity and contributions arising from hydrodynamic, conservative, and contact forces, plotted as a function of dimensionless shear rate for $A = 18$, with (b) $F_A = 0.23F_R$ and (c) $F_A = 0.78F_R$. (d) The average number of fibers in contact as a function of attractive force at $\dot{\gamma}/\dot{\gamma}_0 = 0.02$. For all cases, the volume fraction is fixed to $\phi = 0.17$. As the attractive force increases, the relative viscosity shifts from being dominated by the noncontact interactions to the frictional contacts induced by the attractive force.

be large enough to generate the yield stress, we find that as the attractive force increases, the yield stress shifts from being dominated by the noncontact attraction to frictional contacts generated by the attractive force. Higher attractive forces pull the fibers into more direct contact, as shown in Fig. 6(d), leading to an increase in the yield stress.

The results of this study show that as we change the volume fraction and the attractive force, the material undergoes different rheological states, which can be demonstrated in a flow-state diagram. Using the numerical results in the current work, we generate a flow-state diagram in the $\phi - F_A$ plane for $A = 18$, as shown in Fig. 7. For the range of attractive forces, the suspension is in different states for $\phi < \phi_y^0$, $\phi_y^0 < \phi < \phi_y^m$, and $\phi > \phi_y^m$. Below an attractive force threshold (F_A^0), no yield stress is observed at any volume fraction. Above the threshold of attractive force, the system is in the finite yield stress state for $\phi_y^0 < \phi < \phi_y^m$. Above ϕ_y^0 , the yield stresses increase with ϕ and diverge at ϕ_y^m .

C. Normal stress coefficients

In fiber suspensions, normal stress differences inevitably arise due to the presence of hydrodynamics and interfiber interactions [12]. We compute the first and second normal stress coefficients

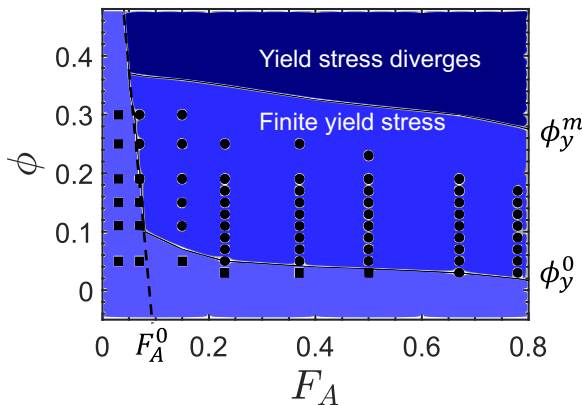


FIG. 7. The flow-state diagram shown for the volume fraction-attractive force plane showing no yield stress (light blue), finite yield stress, and divergence of the yield stress (dark blue). ϕ_y^m line show the limits above which a certain stress have to applied to initiate the flow, and ϕ_y^0 line show the limit above which the yield stress diverges, respectively. The solid white lines are generated by fitting equation (6) with volume fraction vs yield stress data for different attractive forces. The dashed line shows the threshold attractive force (F_A^0), below which no yield stress is observed.

for $A = 10, 18$, and 33 , and compare them with experiments [19] as shown in Fig. 8. The materials and experimental conditions are kept the same as the ones used for the viscosity measurement [10]. Specifically, the experiments are carried out at a higher shear rate when the viscosity reached a plateau. That is why we fix the shear rates to $\dot{\gamma}/\dot{\gamma}_0 = 30$ when the suspension viscosity reaches a plateau in the numerical simulations. All the simulation parameters are the same as in the last section. While the first normal stress coefficient α_1 is positive, the second normal stress coefficient α_2 is negative, in quantitative agreement with the experiments in Refs. [11,12,37]. Moreover, the magnitude of α_2 is smaller than that of α_1 .

In addition, both normal stress coefficients decrease in magnitude with decreasing the aspect ratio, in agreement with the experimental studies in Refs. [11,37]. The origin of the normal stress coefficients at a high shear rate can be better understood by separating the hydrodynamic, contact, and noncontact (attractive+repulsive) contributions to the normal stress coefficient as shown in Figs. 8(c) and 8(d). The hydrodynamic contribution to the normal stress coefficient is negligible for the conditions under consideration. The data presented here clearly show that normal stress coefficients are primarily affected by contact. The normal stress coefficients of suspension increase in magnitude as the volume fraction rise due to an increase in both the contact and noncontact contributions. While the noncontact contribution increases weakly, the contact contribution becomes more significant at a higher volume fraction. Moreover, to investigate the shear rate dependencies, we measure the first and second normal stress coefficients for $A = 18$ and 33 as a function of the shear rate. We observe a similar shear rate dependence for the normal stresses as we do for the viscosity, and the data can be found in Supplemental Material Fig. S5 [42].

D. Effect of coefficient of friction on the normal stress coefficients

We have provided a quantitative explanation of the yield stress, normal stresses, and shear thinning in the fiber suspensions. Our model does an excellent job of reproducing the experimental data. This model can also capture and explain the effect of changing different parameters that control rheology. As an example, we will show the capability of the model to quantify the effect of changing fiber surface properties.

We employed our model to quantify the effect of changing fiber surface properties and compare the results against the experimental observations by Bounoua *et al.* [37]. They changed the surface

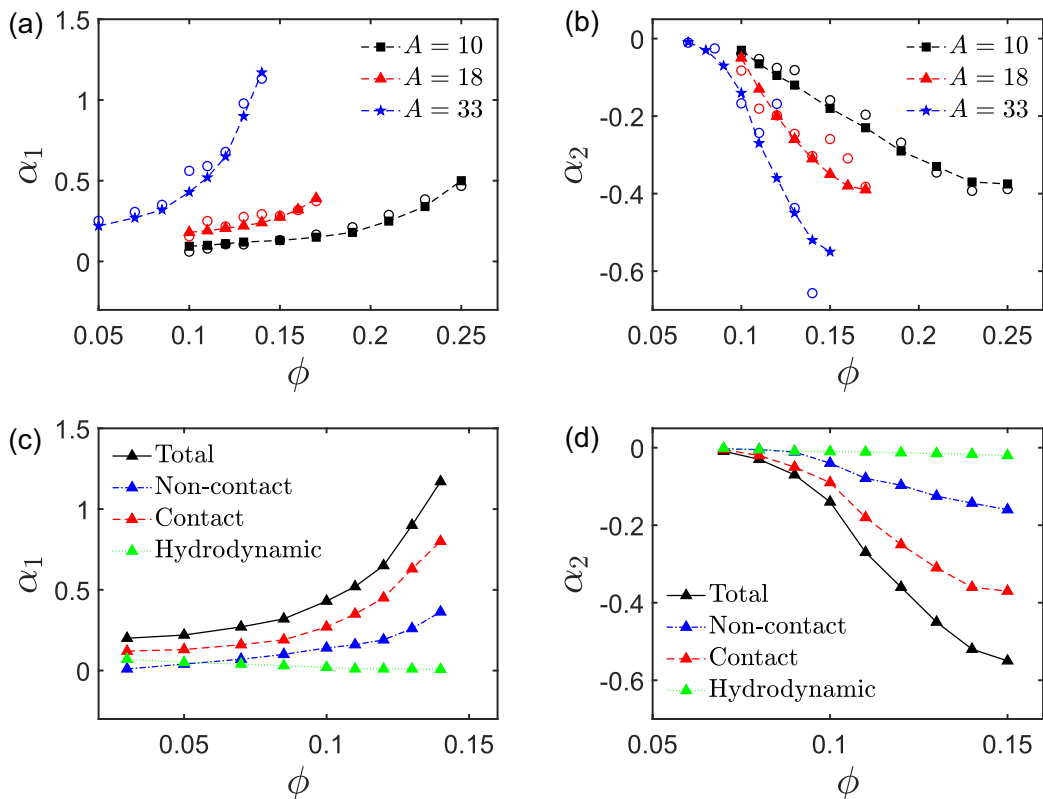


FIG. 8. Numerical and experimental comparison of (a) the first normal stress coefficient α_1 and (b) the second normal stress coefficient α_2 as a function of volume fractions for $A = 10, 18,$ and 33 . Hollow circles correspond to experimental data [19]. Effect of increasing the coefficient of friction μ on contributions arising from hydrodynamic, conservative, and contact forces to the total (c) α_1 , (d) α_2 plotted as a function volume fractions. α_1 is positive and α_2 is negative in agreement with the experiments [11,12,19] at a fixed shear rate $\dot{\gamma}/\dot{\gamma}_0 = 30$ at which the suspension viscosity reached a plateau. The data plotted here demonstrates that the contact contribution is the dominant contributor to the normal stress coefficients at higher shear rates.

properties by washing the fibers. We hypothesize that changing the fiber surface properties will directly modify the solid contact that can be numerically quantified by varying the coefficient of friction. We measure the normal stress coefficients for five different volume fractions ($\phi = 0.10, 0.11, 0.13, 0.14, 0.15$) with aspect ratio $A = 33$, varying the coefficient of friction μ between 0.30 to 0.55. Numerical results, having $\mu = 0.40$ and 0.48 , match closely with the experiment for washed and unwashed fibers, respectively, as shown in Figs. 9(a) and 9(b). These results demonstrate the applicability of the proposed model to capture and quantify the effect of modifying fiber surface properties.

The effect of friction is more pronounced on $|\alpha_1|$ compared to $|\alpha_2|$. To understand the underlying mechanism of the effect of modifying solid contact between fibers, we examine the hydrodynamic, contact, and noncontact contributions to the normal stress coefficients for $\mu = 0.40$ (filled symbols) and $\mu = 0.55$ (hollow symbols) in Figs. 9(c) and 9(d). We observe that the hydrodynamics contribution is almost independent of the friction coefficient. While the noncontact contribution increases weekly, the contact contribution increases significantly for the first normal stress coefficient α_1 . The noted increase in the magnitude of α_1 is, therefore, solely due to the increase in the contact contribution. For the second normal stress coefficient α_2 in Fig. 9(d), a similar conclusion holds:

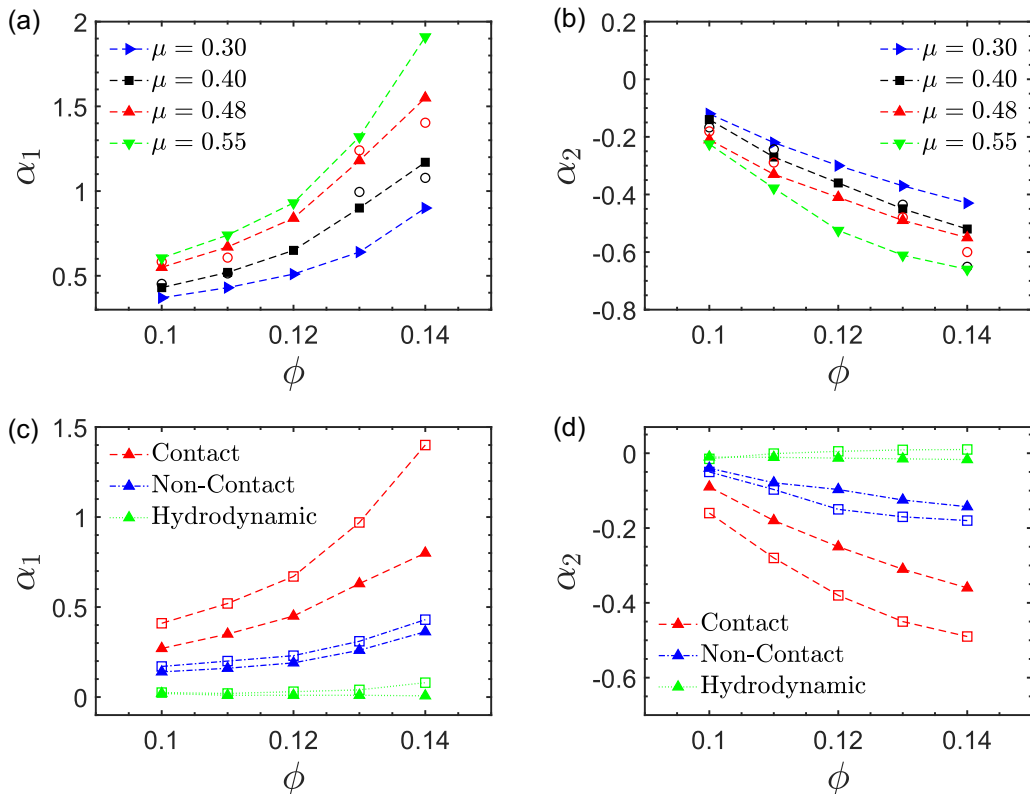


FIG. 9. (a) First normal stress coefficients α_1 and (b) second normal stress coefficient α_2 as a function of volume fraction ϕ for different values of friction coefficient μ . Filled symbols with dashed lines show the numerical data. The black and red hollow circles show experimental values for unwashed and washed fibers, respectively [19]. The aspect ratio of the fibers was fixed to $A = 33$. The effect of friction on the normal stress coefficients is significant, with a rise in $|\alpha_1|$ and $|\alpha_2|$. Hydrodynamic, contact, and noncontact contributions to (c) first normal stress coefficient α_1 and (d) second normal stress coefficient α_2 as a function of volume fraction ϕ for friction coefficient $\mu = 0.40$ (filled symbols) and $\mu = 0.55$ (hollow symbols). As the volume fraction increases, the contact contribution increases significantly, leading to an increase in the magnitude of the normal stress coefficients.

the friction weakly affects the hydrodynamic and noncontact contributions while it significantly increases the contact contribution.

IV. CONCLUSION

Our research provides fundamental insights into the complex rheological behavior of fiber suspensions based on balances between hydrodynamic, conservative, and contact forces. In this work, we provided the first quantitative explanation of the origin of yield stress, shear thinning, and normal stress differences in fiber suspensions by focusing on contact and noncontact contributions. Comparing the relative viscosity, the first normal stress coefficient α_1 , and the second normal stress coefficient α_2 with experimental measurements corroborate the proposed model. We demonstrated that the attractive interaction of van der Waals origin results in yield stress. Moreover, we explored the divergence of the yield stress as the suspension volume fraction, ϕ approaches the maximum flowable limit, ϕ_y^m . Rescaling volume fraction, ϕ by the jamming volume fraction, ϕ_y^m collapsed the yield stress data for varying aspect ratios on a single curve, denoting that changing the fiber

aspect ratio affects the maximum volume fraction at which the yield stress diverges. In addition, we demonstrated that the degree of shear thinning and yield stress depends on the strength of attractive force, which can be regulated in principle by fiber size, microstructure, chemistry at solid-fluid interfaces, and fluid and solid phase parameters such as dielectric properties [65,66].

The first and second normal stress coefficients were compared with experiments for different aspect ratios and volume fractions to explore the dilute, semidilute, and concentrated regimes. The results showed that the first normal stress coefficient α_1 is positive and the second normal stress coefficient α_2 is negative, in agreement with available experiments [11,12,19]. As expected, the contact contribution is the dominant contribution to the normal stress differences at higher shear rates because noncontact contributions become less and less important as the shear rate increases.

A direct comparison of normal stress coefficients with the experiment was performed when the fiber surface was modified. We captured the impact of changing fiber properties by modifying the frictional contact by changing the coefficient of friction. Interestingly, the friction appeared to act primarily through the contact stresses, as the hydrodynamic and noncontact stresses were unaffected by friction. Our results demonstrated the importance of accurately modeling the interfiber interactions to capture the experimentally observed shear-rate-dependent rheological behavior of fiber suspensions. Due to the complexity of attractive and friction forces at the microscopic scale and the number of parameters that are potentially relevant in the surface physical chemistry, the next step would be to quantitatively determine the attractive and frictional force from colloidal probe AFM measurements.

ACKNOWLEDGMENT

A.M.A. acknowledges financial support from the Department of Energy via Grant No. EE0008910.

-
- [1] C. H. Bivins, C. Boney, C. Fredd, J. Lassek, P. Sullivan, J. Engels, E. O. Fielder, T. Gorham, T. Judd, A. E. S. Mogollon *et al.*, New fibers for hydraulic fracturing, *Oilfield Rev.* **17**, 34 (2005).
 - [2] R. Elgaddafi, R. Ahmed, M. George, and F. Growcock, Settling behavior of spherical particles in fiber-containing drilling fluids, *J. Pet. Sci. Eng.* **84-85**, 20 (2012).
 - [3] M. Hassanpour, P. Shafigh, and H. B. Mahmud, Lightweight aggregate concrete fiber reinforcement—A review, *Construction Build. Mater.* **37**, 452 (2012).
 - [4] F. Lundell, L. D. Söderberg, and P. H. Alfredsson, Fluid mechanics of papermaking, *Annu. Rev. Fluid Mech.* **43**, 195 (2011).
 - [5] S. B. Lindström and T. Uesaka, Simulation of semidilute suspensions of non-Brownian fibers in shear flow, *J. Chem. Phys.* **128**, 024901 (2008).
 - [6] M. Nawab and S. Mason, Viscosity of dilute suspensions of threadlike particles, *J. Phys. Chem.* **62**, 1248 (1958).
 - [7] J. Mewis and A. Metzner, The rheological properties of suspensions of fibres in Newtonian fluids subjected to extensional deformations, *J. Fluid Mech.* **62**, 593 (1974).
 - [8] T. Kitano and T. Kataoka, The rheology of suspensions of vinylon fibers in polymer liquids. I. Suspensions in silicone oil, *Rheol. Acta* **20**, 390 (1981).
 - [9] S. Goto, H. Nagazono, and H. Kato, The flow behavior of fiber suspensions in Newtonian fluids and polymer solutions, *Rheol. Acta* **25**, 119 (1986).
 - [10] S. Bounoua, E. Lemaire, J. Férec, G. Ausias, and P. Kuzhir, Shear-thinning in concentrated rigid fiber suspensions: Aggregation induced by adhesive interactions, *J. Rheology* **60**, 1279 (2016).
 - [11] B. Snook, L. M. Davidson, J. E. Butler, O. Pouliquen, and E. Guazzelli, Normal stress differences in suspensions of rigid fibres, *J. Fluid Mech.* **758**, 486 (2014).

- [12] M. Keshtkar, M. Heuzey, and P. Carreau, Rheological behavior of fiber-filled model suspensions: Effect of fiber flexibility, *J. Rheology* **53**, 631 (2009).
- [13] D. Quemada and C. Berli, Energy of interaction in colloids and its implications in rheological modeling, *Adv. Colloid Interface Sci.* **98**, 51 (2002).
- [14] S. R. Raghavan and J. F. Douglas, The conundrum of gel formation by molecular nanofibers, wormlike micelles, and filamentous proteins: Gelation without cross-links? *Soft Matter* **8**, 8539 (2012).
- [15] C. Bennington, R. Kerekes, and J. Grace, The yield stress of fibre suspensions, *Can. J. Chem. Eng.* **68**, 748 (1990).
- [16] Y. S. Song and J. R. Youn, Influence of dispersion states of carbon nanotubes on physical properties of epoxy nanocomposites, *Carbon* **43**, 1378 (2005).
- [17] W. Ma, F. Chinesta, A. Ammar, and M. Mackley, Rheological modeling of carbon nanotube aggregate suspensions, *J. Rheology* **52**, 1311 (2008).
- [18] G. Natale, M. Heuzey, P. Carreau, G. Ausias, and J. Férec, Rheological modeling of carbon nanotube suspensions with rod-rod interactions, *AIChE J.* **60**, 1476 (2014).
- [19] S. Bounoua, P. Kuzhir, and E. Lemaire, Normal stress differences in non-Brownian fiber suspensions, *J. Rheol.* **60**, 661 (2016).
- [20] A. Singh, S. Pednekar, J. Chun, M. M. Denn, and J. F. Morris, From Yielding to Shear Jamming in a Cohesive Frictional Suspension, *Phys. Rev. Lett.* **122**, 098004 (2019).
- [21] M. Khan, R. V. More, A. A. Banaei, L. Brandt, and A. M. Ardekani, Rheology of concentrated fiber suspensions with a load-dependent friction coefficient, *Phys. Rev. Fluids* **8**, 044301 (2023).
- [22] L. Lobry, E. Lemaire, F. Blanc, S. Gallier, and F. Peters, Shear thinning in non-Brownian suspensions explained by variable friction between particles, *J. Fluid Mech.* **860**, 682 (2019).
- [23] J. Wu and C. K. Aidun, A numerical study of the effect of fibre stiffness on the rheology of sheared flexible fibre suspensions, *J. Fluid Mech.* **662**, 123 (2010).
- [24] A. A. Banaei, M. E. Rosti, and L. Brandt, Numerical study of filament suspensions at finite inertia, *J. Fluid Mech.* **882**, A5 (2020).
- [25] R. V. More and A. M. Ardekani, A unifying mechanism to explain the rate-dependent rheological behavior in non-Brownian suspensions: One curve to unify them all, *Phys. Rev. E* **103**, 062610 (2021).
- [26] É. Guazzelli and O. Pouliquen, Rheology of dense granular suspensions, *J. Fluid Mech.* **852**, P1 (2018).
- [27] M. Djalili-Moghaddam and S. Toll, Fibre suspension rheology: Effect of concentration, aspect ratio, and fibre size, *Rheol. Acta* **45**, 315 (2006).
- [28] J. Férec, G. Ausias, M. Heuzey, and P. Carreau, Modeling fiber interactions in semiconcentrated fiber suspensions, *J. Rheol.* **53**, 49 (2009).
- [29] L. H. Switzer III and D. J. Klingenberg, Rheology of sheared flexible fiber suspensions via fiber-level simulations, *J. Rheol.* **47**, 759 (2003).
- [30] B. J. Maranzano and N. J. Wagner, The effects of interparticle interactions and particle size on reversible shear thickening: Hard-sphere colloidal dispersions, *J. Rheol.* **45**, 1205 (2001).
- [31] V. Gopalakrishnan and C. Zukoski, Effect of attractions on shear thickening in dense suspensions, *J. Rheol.* **48**, 1321 (2004).
- [32] E. Brown, N. A. Forman, C. S. Orellana, H. Zhang, B. W. Maynor, D. E. Betts, J. M. DeSimone, and H. M. Jaeger, Generality of shear thickening in dense suspensions, *Nat. Mater.* **9**, 220 (2010).
- [33] M. Solomon and D. Boger, The rheology of aqueous dispersions of spindle-type colloidal hematite rods, *J. Rheol.* **42**, 929 (1998).
- [34] L. J. Michot, C. Baravian, I. Bihannic, S. Maddi, C. Moyne, J. F. Duval, P. Levitz, and P. Davidson, Sol-gel and isotropic/nematic transitions in aqueous suspensions of natural nontronite clay. Influence of particle anisotropy. 2. Gel structure and mechanical properties, *Langmuir* **25**, 127 (2009).
- [35] M. Chauche and D. L. Koch, Rheology of non-Brownian rigid fiber suspensions with adhesive contacts, *J. Rheol.* **45**, 369 (2001).
- [36] L. Bergström, Shear thinning and shear thickening of concentrated ceramic suspensions, *Colloids Surf. A* **133**, 151 (1998).
- [37] S. Bounoua, E. Lemaire, J. Férec, G. Ausias, A. Zubarev, and P. Kuzhir, Apparent yield stress in rigid fibre suspensions: The role of attractive colloidal interactions, *J. Fluid Mech.* **802**, 611 (2016).

- [38] F. Tapia, S. Shaikh, J. E. Butler, O. Pouliquen, and É. Guazzelli, Rheology of concentrated suspensions of noncolloidal rigid fibres, *J. Fluid Mech.* **827**, R5 (2017).
- [39] W.-X. Huang, S. J. Shin, and H. J. Sung, Simulation of flexible filaments in a uniform flow by the immersed boundary method, *J. Comput. Phys.* **226**, 2206 (2007).
- [40] A. Pinelli, M. Omidyeganeh, C. Brücker, A. Revell, A. Sarkar, and E. Alinovi, The pelskin project: Part iv-control of bluff body wakes using hairy filaments, *Meccanica* **52**, 1503 (2017).
- [41] C. S. Peskin, Flow patterns around heart valves: A numerical method, *J. Comput. Phys.* **10**, 252 (1972).
- [42] See Supplemental Material at <http://link.aps.org/supplemental/10.1103/PhysRevFluids.8.064306> for methods and Supplemental data. We provide details about the numerical method used in these simulations. We provide further evidence in support of our model by comparing high shear rate viscosity for a range of volume fractions. At the end, we report the shear rate dependent normal stresses, and nematic order parameter in the fiber suspension.
- [43] Y. Yamane, Y. Kaneda, and M. Dio, Numerical simulation of semidilute suspensions of rodlike particles in shear flow, *J. Non-Newtonian Fluid Mech.* **54**, 405 (1994).
- [44] J. N. Israelachvili, *Intermolecular and Surface Forces* (Academic Press, San Diego, CA, 2011).
- [45] S. Gallier, E. Lemaire, F. Peters, and L. Lobry, Rheology of sheared suspensions of rough frictional particles, *J. Fluid Mech.* **757**, 514 (2014).
- [46] R. More and A. Ardekani, A constitutive model for sheared dense suspensions of rough particles, *J. Rheol.* **64**, 1107 (2020).
- [47] R. More and A. Ardekani, Roughness induced shear thickening in frictional non-Brownian suspensions: A numerical study, *J. Rheol.* **64**, 283 (2020).
- [48] R. V. More and A. M. Ardekani, Effect of roughness on the rheology of concentrated non-Brownian suspensions: A numerical study, *J. Rheol.* **64**, 67 (2020).
- [49] R. I. Tanner and S. Dai, Particle roughness and rheology in noncolloidal suspensions, *J. Rheol.* **60**, 809 (2016).
- [50] C. P. Broedersz and F. C. MacKintosh, Modeling semiflexible polymer networks, *Rev. Mod. Phys.* **86**, 995 (2014).
- [51] F. P. Bowden and D. Tabor, *The Friction and Lubrication of Solids-Part II* (Oxford University Press, Oxford, UK, 1964).
- [52] M. P. Petrich and D. L. Koch, Interactions between contacting fibers, *Phys. Fluids* **10**, 2111 (1998).
- [53] M. Fujita and Y. Yamaguchi, Simulation model of concentrated colloidal nanoparticulate flows, *Phys. Rev. E* **77**, 026706 (2008).
- [54] G. Batchelor, The stress generated in a nondilute suspension of elongated particles by pure straining motion, *J. Fluid Mech.* **46**, 813 (1971).
- [55] L. Onsager, The effects of shape on the interaction of colloidal particles, *Ann. N.Y. Acad. Sci.* **51**, 627 (1949).
- [56] T. Odijk, Theory of lyotropic polymer liquid crystals, *Macromolecules* **19**, 2313 (1986).
- [57] G. J. Vroege and H. N. Lekkerkerker, Phase transitions in lyotropic colloidal and polymer liquid crystals, *Rep. Prog. Phys.* **55**, 1241 (1992).
- [58] A. P. Philipse, The random contact equation and its implications for (colloidal) rods in packings, suspensions, and anisotropic powders, *Langmuir* **12**, 1127 (1996).
- [59] Y. Xu, A. Atrens, and J. R. Stokes, A review of nanocrystalline cellulose suspensions: Rheology, liquid crystal ordering and colloidal phase behavior, *Adv. Colloid Interface Sci.* **275**, 102076 (2020).
- [60] H. W. Hatch, N. A. Mahynski, R. P. Murphy, M. A. Blanco, and V. K. Shen, Monte Carlo simulation of cylinders with short-range attractions, *AIP Adv.* **8**, 095210 (2018).
- [61] J. Z. Zhou, P. H. Uhlherr, and F. T. Luo, Yield stress and maximum packing fraction of concentrated suspensions, *Rheol. Acta* **34**, 544 (1995).
- [62] A. P. Philipse and A. M. Wierenga, On the density and structure formation in gels and clusters of colloidal rods and fibers, *Langmuir* **14**, 49 (1998).
- [63] M. J. Solomon and P. T. Spicer, Microstructural regimes of colloidal rod suspensions, gels, and glasses, *Soft Matter* **6**, 1391 (2010).

- [64] S. R. Williams and A. P. Philipse, Random packings of spheres and spherocylinders simulated by mechanical contraction, [Phys. Rev. E **67**, 051301 \(2003\)](#).
- [65] P. J. Scales, S. B. Johnson, T. W. Healy, and P. C. Kapur, Shear yield stress of partially flocculated colloidal suspensions, [AIChE J. **44**, 538 \(1998\)](#).
- [66] L. Oyarte Gálvez, S. de Beer, D. van der Meer, and A. Pons, Dramatic effect of fluid chemistry on corn-starch suspensions: Linking particle interactions to macroscopic rheology, [Phys. Rev. E **95**, 030602\(R\) \(2017\)](#).